Supporting Information

A Degradation-Free Platform for Intrinsic Comparison of Metal Nanoparticles in Methane-Fueled SOFC Anodes

Calem Duah[a,b†], SungHyun Jeon[c,d†], Raphael Edem Agbenyeke[a,b], Jongsu Seo[e], Chang Gyoun Kim[a], Young Kuk Lee[a], Seon Joo Lee[a,b*], and WooChul Jung[c,f*]

[a] Advanced Materials Division, Korea Research Institute of Chemical Technology (KRICT), Daejeon 34114, Republic of Korea.

[b] Department of Advanced Materials and Chemical Engineering, University of Science and Technology (UST), Daejeon 34113, Republic of Korea

[c] Research Institute of Advanced Materials, Seoul National University (SNU), Seoul 08826, Republic of Korea

[d] Current address: Department of Materials Science and Engineering, Northwestern University, Evanston, IL, 60201, USA

[e] Hydrogen Research Department, Korea Institute of Energy Research (KIER), Daejeon 34129, Republic of Korea

[f] Department of Materials Science and Engineering, Seoul National University (SNU), Seoul 08826, Republic of Korea

† These authors contributed equally to this work.

***Corresponding Authors**

Email: sjlee614@krict.re.kr, wcjung@snu.ac.kr

EXPERIMENTAL SECTION

Materials

Platinum acetylacetonate ($Pt(acac)_2$, 97%), Nickel (II) acetylacetonate ($Ni(acac)_2$, 95%), Ruthenium (III) acetylacetonate ($Ru(acac)_3$, 97%), Oleylamine (OAm, $C_{18}H_{35}NH_2$, 70%), Oleic Acid (OA, $C_{17}H_{33}COOH$, 90%), 1-Octadecene (90%), Ethylene glycol (EG, 99.8%), Trioctylphosphine (TOP, 90%), Polyvinylpyrrolidone (PVP, $(C_6H_9NO)n$, MW ~55k), 11-mercaptoundecanoic acid (MUA, 95%), 3-mercaptopropionic acid (MPA, ≥99%), 4-mercaptophenol (MP, 97%), 3-mercaptobenzoic acid (MBA, 95%) and Iron (0) Pentacarbonyl ($Fe(CO)_5$) were purchased from Sigma-Aldrich. Hexane, Ethanol, Methanol, Acetone, Isopropyl alcohol was purchased from Samchun Chemicals. All chemicals were used without further purification.

Synthesis of platinum nanoparticles

Platinum nanoparticles were synthesized using a modified literature procedure. [1] All reactions were carried out under a nitrogen atmosphere using standard Schlenk line techniques. In a 100 mL flask, $Pt(acac)_2$ (0.1 g, 0.25 mmol), ODE (10 mL), OA (1 mL), and OAm (1 mL) were mixed under magnetic stirring. The mixture was then heated to 90 °C under vacuum for 1 h to dissolve $Pt(acac)_2$. The temperature was then raised to 180 °C under N_2 flow and 0.1 mL of a solution of $Fe(CO)_5$ in hexane (prepared from 0.1 mL $Fe(CO)_5$ in 1 mL hexane) was quickly injected into the hot solution. The solution was kept at this temperature for 5 minutes before it was quenched by the addition of 40 mL of isopropyl alcohol (IPA). The solution was then centrifuged (10000 rpm, 10 min) to precipitate and separate the nanoparticles. The resulting mixture was washed twice with hexane (6 mL) and ethanol (30 mL) using centrifugation (10,000 rpm, 10 min) to remove impurities and excess reagents, and the final product was dispersed in 5 mL of hexane.

Synthesis of ruthenium nanoparticles

Ruthenium nanoparticles were synthesized using a modified literature procedure. [2] All reactions were conducted under a nitrogen atmosphere using standard Schlenk line techniques. In a typical synthesis, $Ru(acac)_3$ (0.1 g, 0.25 mmol), EG (5 mL), and PVP (0.01 g), were mixed in a 100 mL flask under magnetic stirring. The mixture was

degassed at 120 °C for 30 minutes and then heated to 180 °C under N_2 flow and maintained at this temperature for 3 h. The solution was quenched in an ice-water bath and 40 mL of acetone was added and then centrifuged (10000 rpm, 10 min) to rinse and separate the nanoparticles. For the ligand exchange process, the supernatant was discarded and the separated nanoparticle precipitate in the centrifuge tube was further used. Otherwise, the separated nanoparticle was re-dispersed in 10 mL methanol.

Ligand exchange on ruthenium nanoparticles

Following a previously reported protocol, [3] 50 mg of MUA was dissolved in 5 mL of methanol (or 20 µL for MPA, 35.3 mg for MBA, 28.9 mg for MP) and tetramethylammonium hydroxipentahydrate was added dropwise until the pH reached 11. Then, 4 mL of the ligand solution was added to the Ru NP precipitate in the centrifuge tube and sonicated for 5 secs. The resulting dispersion was precipitated again by the addition of 30 mL of toluene, followed by centrifugation at 10,000 rpm for 5 min. The precipitate was then redispersed in 2.5 mL of methanol.

Synthesis of nickel nanoparticles

Nickel nanoparticles were synthesized using a modified literature procedure. [4] All reactions were conducted under a nitrogen atmosphere using standard Schlenk line techniques. $Ni(acac)_2$ (0.162 g, 0.63 mmol), OAm (8 mL) and TOP (2 mL), were mixed under N_2 and magnetic stirring. The mixture was then heated to 215 °C and held for 30 min. The solution was quenched by slowly adding 40 mL of ethanol and the centrifuged (10000 rpm, 10 min) to wash and separate the nanoparticles. The final product was dispersed in 5 mL of hexane after washing twice with hexane/ethanol.

Drop-assisted immersion coating

0.2 mL of concentrated nanoparticle dispersion was diluted into 15 mL of solvent (hexane for Pt and Ni, methanol for Ru) and mixed to ensure homogeneity. The PBMO substrate was placed in a 60 mm diameter Petri dish, after which the diluted NP solution was added dropwise until the substrate was fully submerged. The system was left undisturbed for 2 h to allow uniform coating of the nanoparticles throughout the porous architecture, after which the substrate was

removed and air-dried under ambient conditions for 1 h.

Cell preparation

To prepare symmetrical half-cells, the synthesized PBMO powder was mixed with ethanol and an ink vehicle (Fuel Cell Materials Co.) via ball milling to produce a slurry. The PBMO slurry was then screen-printed onto both sides of a 1 cm x 1 cm Y_2O_3-stabilized ZrO_2 ($Y_{0.08}Zr_{0.92}O_{1.96}$, YSZ) electrolyte with thickness of around 25 μm. To prevent a side reaction at the YSZ electrolyte and PBMO, a Gd-doped CeO_2 ($Ce_{0.9}Gd_{0.1}O_{1.95}$, GDC) interlayer was deposited via Pulse Layer Deposition (PLD) followed by sintered at 950 ^oC for one hour, to ensure adhesion.

Atomic layer deposition

Thin Al_2O_3 overlayer was deposited using trimethylaluminum (TMA) as the Al precursor and water as the oxidant at 150 °C for 20 cycles. A typical cycle followed the sequence: Al precursor dose (0.2 s) – Ar purge (15 s) – water dose (0.2 s) – Ar purge (15 s).

Thin ZnO overlayer was deposited using diethylzinc (DEZ) as the Zn precursor and water as the oxidant at 140 °C for 10 cycles. A typical cycle followed the sequence: Zn precursor dose (1.2 s) – Ar purge (30 s) – water dose (0.5 s) – Ar purge (60 s).

Characterization

The size and morphology of the nanoparticles were assessed using high-resolution transmission electron microscopy (HRTEM, F200S, Talos) operated at an accelerating voltage of 200 kV, equipped with EDX for elemental mapping. For TEM analysis, diluted nanoparticle dispersions were drop-cast onto carbon-coated copper grids. The crystal structure of the NPs was investigated using X-ray diffraction (XRD, SmartLab, Rigaku) with a Cu Kα source (l = 1.5418Å) operated at 40 kV and 40 mA. NP-decorated structures were examined using high-resolution field emission scanning electron microscopy (FE-SEM, Carl Zeiss, Sigma HD). The chemical composition and oxidation states of pristine and NP-decorated PBMO samples were analyzed using *in situ* X-ray photoelectron spectroscopy (XPS, Axis-Supra, Kratos), with measurements conducted at 700 °C, under ultra-high vacuum conditions (below 10^{-8} mbar). The

fitting of XPS spectra was conducted using Casa XPS software for better chemical quantification. Electrochemical performance was assessed using symmetric cells configured as PBMO|GDC|YSZ|GDC|PBMO. Impedance spectra were acquired via electrochemical impedance spectroscopy (EIS, VSP-300, BioLogic) within a custom-built fuel cell test station operating at 600 – 700 °C. During measurements, wet (3% H_2O) CH_4 was delivered at a constant total flow rate of 100 sccm using mass flow controllers. Short-term stability testing was performed under a constant voltage load of 0.65 V at 700 °C. Distribution of relaxation time (DRT) analysis was conducted with DRT tools and software obtained from Ciucci's group. [5]

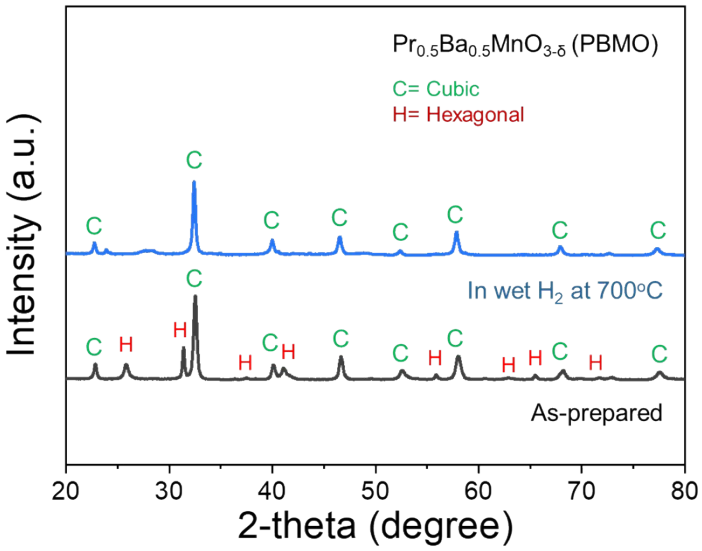

Figure S1. X-ray diffraction (XRD) pattern of $Pr_{0.5}Ba_{0.5}MnO_{3-\delta}$ anode in the as-prepared state and after treatment in H_2 at 700 °C.

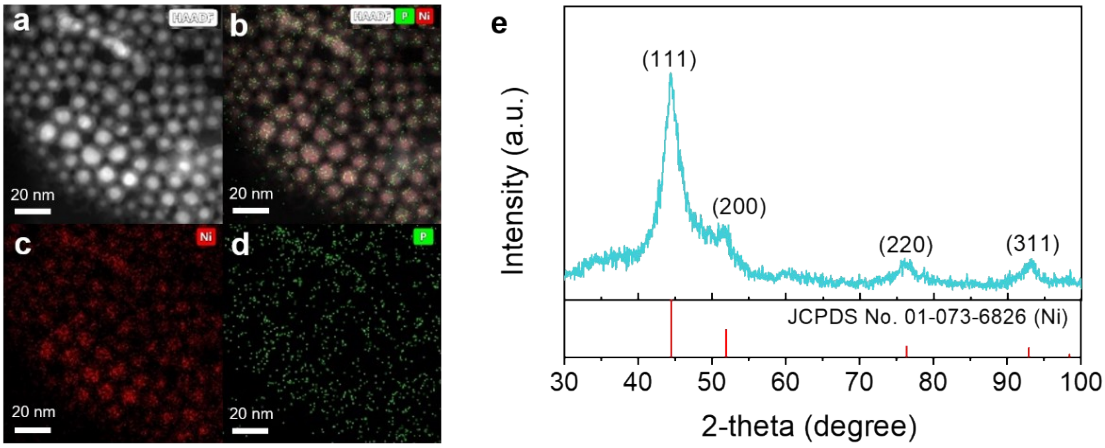

Figure S2. (a) HAADF-STEM, (c–d) corresponding elemental mapping images and (e) XRD pattern of colloidally synthesized Ni nanoparticles.

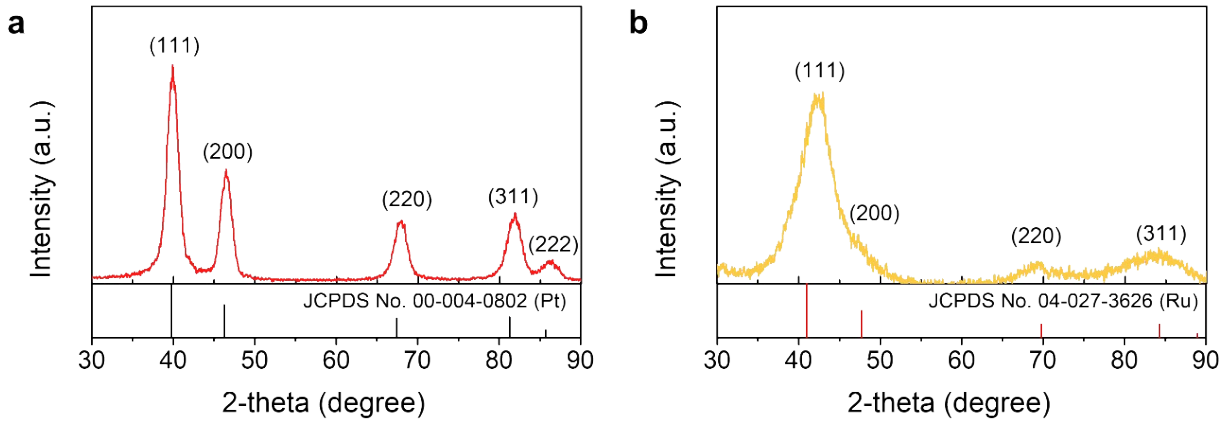

Figure S3. XRD patterns of synthesized (a) Pt and (b) Ru nanoparticles.

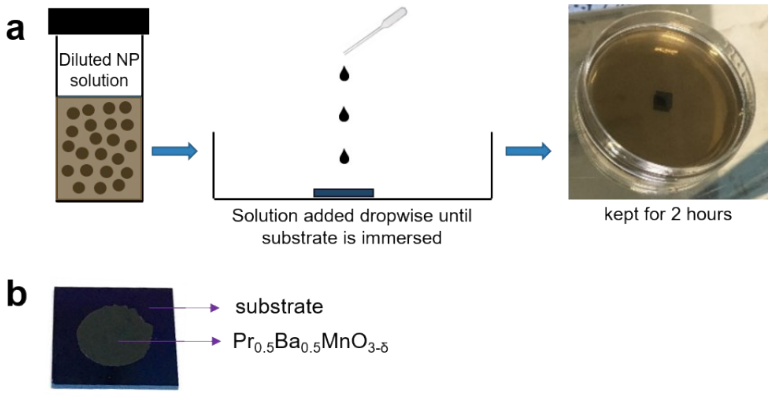

Figure S4. (a) schematic illustration of the solution-based drop-assisted immersion coating technique used in this study. (b) Image of $Pr_{0.5}Ba_{0.5}MnO_{3-\delta}$ screen-printed onto a 1 cm x 1 cm substrate.

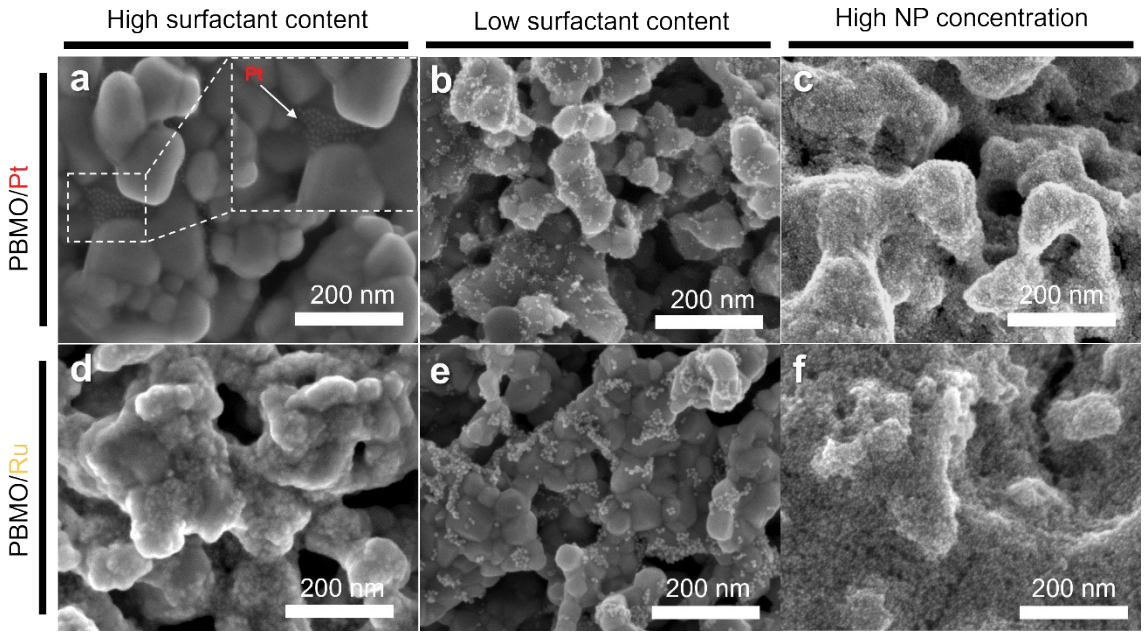

Figure S5. SEM images of (a–c) PBMO/Pt and (d–f) PBMO/Ru electrodes prepared using colloidal solutions with (a, d) high surfactant content, (b, e) low surfactant content, and (c, f) highly concentrated nanoparticles.

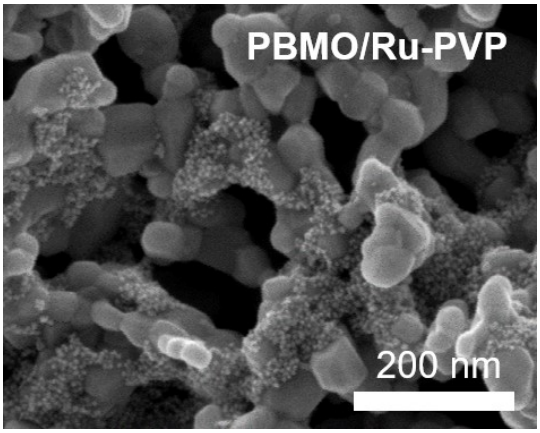

Figure S6. SEM image of PBMO/Ru-PVP electrodes before ligand exchange.

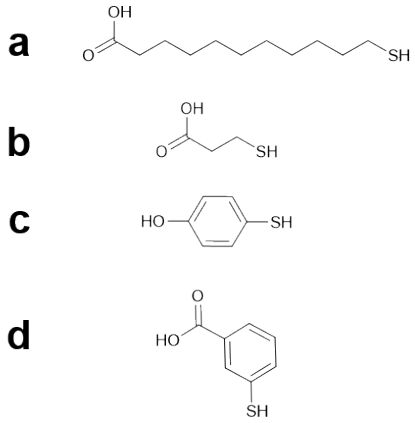

Chart S1. Chemical structures of (a) 11-mercaptoundecanoic acid (MUA), (b) 3-mercaptopropionic acid (MPA), (c) 4-mercaptophenol (MP), and (d) 3-mercaptobenzoic acid (MBA)

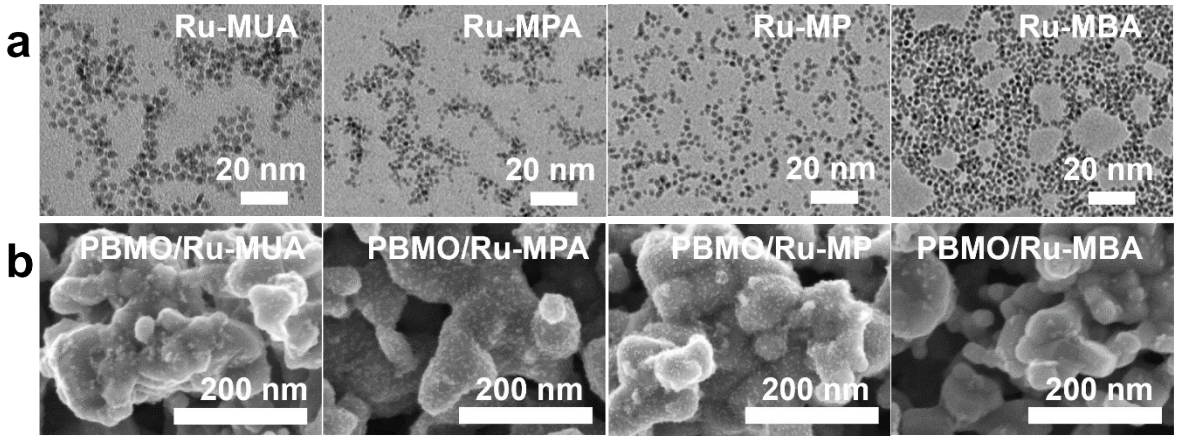

Figure S7. (a) TEM images of Ru nanoparticles following ligand exchange with various thiol-based ligands. (b) SEM images of the corresponding Ru nanoparticles from (a) deposited onto PBMO.

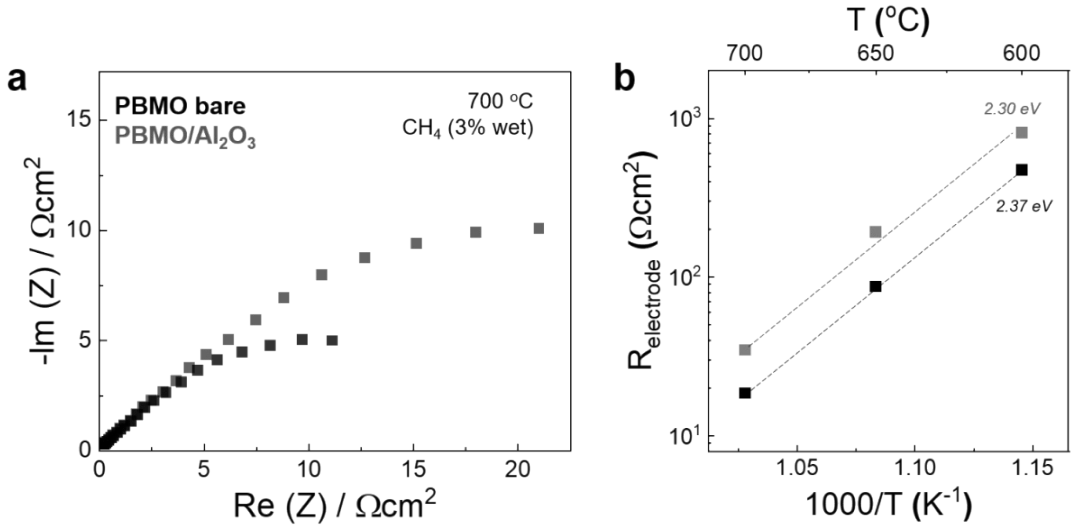

Figure S8. Comparison results between bare PBMO and PBMO/Al_2O_3. (a) Nyquist plot at 700 °C and (b) Arrhenius plot.

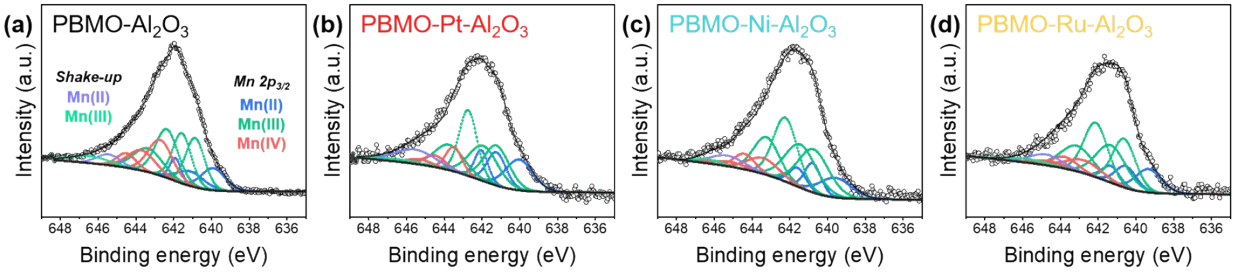

Figure S9. XPS scans of the Mn $2p_{3/2}$ core-level peak spectra recorded from (a) bare PBMO/Al_2O_3 (b) PBMO/Pt/Al_2O_3 (c) PBMO/Ni/Al_2O_3, and (d) PBMO/Ru/Al_2O_3 samples.

Table S1. Mn $2p_{3/2}$ fitting parameters (peak position, fraction, and Δ) for Mn (II-IV) and corresponding shake-up peaks of Figure S8.

Compound	Peak 1 (Position)	Fraction (%)	Peak 2 Δ(Peak 2-Peak 1)	Fraction (%)	Peak 3 Δ(Peak 3-Peak 1)	Fraction (%)	Peak 4 Δ(Peak 4-Peak 1)	Fraction (%)
Mn(II)	640.3 ± 0.5 eV	44.4	1.2 eV	33.8	2.0 eV	21.8		
Mn(III)	641.2 ± 0.5 eV	25.7	0.7 eV	25.7	1.5 eV	29.8	2.5 eV	18.8
Mn(IV)	643.0 ± 0.5 eV	51.1	1.0 eV	32.6	1.8 eV	16.3		
Mn(II) Shake-up	645.5 ± 0.2 eV							
Mn(III) Shake-up	646.5 ± 0.2 eV							

Table S2. Summarized XPS fitting on Mn $2p_{3/2}$ spectra for (a) PBMO-Al_2O_3, (b) PBMO-Pt- Al_2O_3, (c) PBMO-Ni-Al_2O_3, and (d) PBMO-Ru-Al_2O_3 as depicted on Figure S8.

Samples	Mn(II) $2p_{3/2}$	Mn(III) $2p_{3/2}$	Mn(IV) $2p_{3/2}$	Mn(II) Shake-up	Mn(III) Shake-up	Total Mn Oxidation State
Bare	16.7 %	52.0%	24.0%	3.5%	3.8%	**+3.04**
Pt	25.8%	54.1%	10.6%	4.2%	1.7%	**+2.77**
Ni	17.6%	64.7%	12.1%	4.4%	1.2%	**+2.90**
Ru	19.0%	61.5%	11.7%	4.9%	2.0%	**+2.87**

The interfacial chemical environment of Al_2O_3-coated and nanoparticle-functionalized PBMO electrodes was investigated using X-ray photoelectron spectroscopy (XPS). **Figure S9** shows comparison of Mn 2p spectra of four representative samples in this study. The XPS deconvolution was conducted using the fitting parameters summarized in **Table S1**. Specifically, the Mn $2p_{3/2}$ spectra was fitted with three peaks for Mn(II), four peaks for Mn(III), and three

peaks for Mn(IV), each constrained by the fixed fractional ratio and energy separation (Δ) derived from reference data. [6–9] In addition, two shake-up peaks corresponding to Mn(II) and Mn(III) were included. [10]

The relative proportions of Mn oxidation states obtained from the fittings for PBMO-Al_2O_3, PBMO-Pt-Al_2O_3, PBMO-Ni-Al_2O_3, PBMO-Ru-Al_2O_3 were summarized in **Table S2**. A clear increase in Mn(II) component was observed upon nanoparticle incorporation, indicating partial reduction of Mn species at the electrode surface. [11] Consequently, the average Mn oxidation states were calculated to be +3.04, +2.90, +2.87, and +2.77 for the bare, Ni-, Ru-, and Pt-modified samples, respectively. Considering the critical role of Mn oxidation state in determining the catalytic activities, [12,13] these findings are consistent with the electrochemical impedance spectroscopy (EIS) results shown in **Figure 5** in the main text.

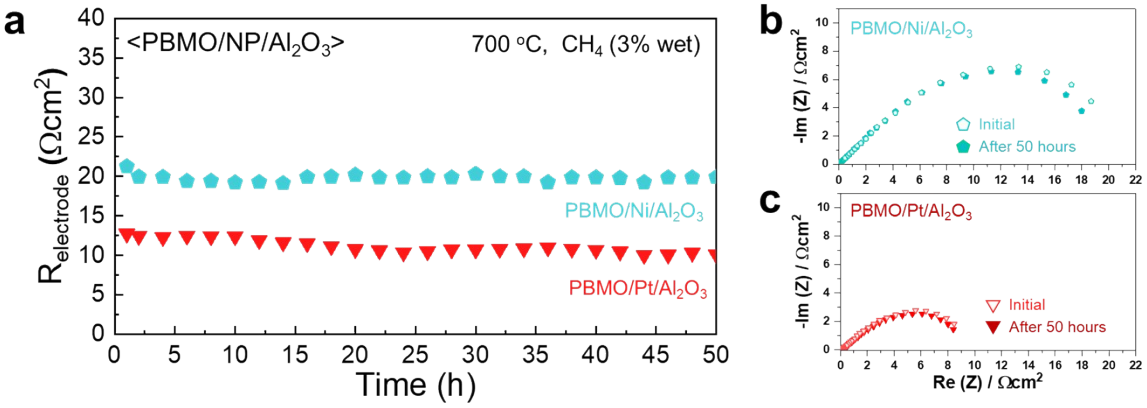

Figure S10. Stability test results of PBMO/Ni/Al_2O_3 and PBMO/Pt/Al_2O_3 over 50 h of operation. (a) Resistance change over time and (b-c) corresponding Nyquist plot of (b) PBMO/Ni/Al_2O_3 and (c) PBMO/Pt/Al_2O_3.

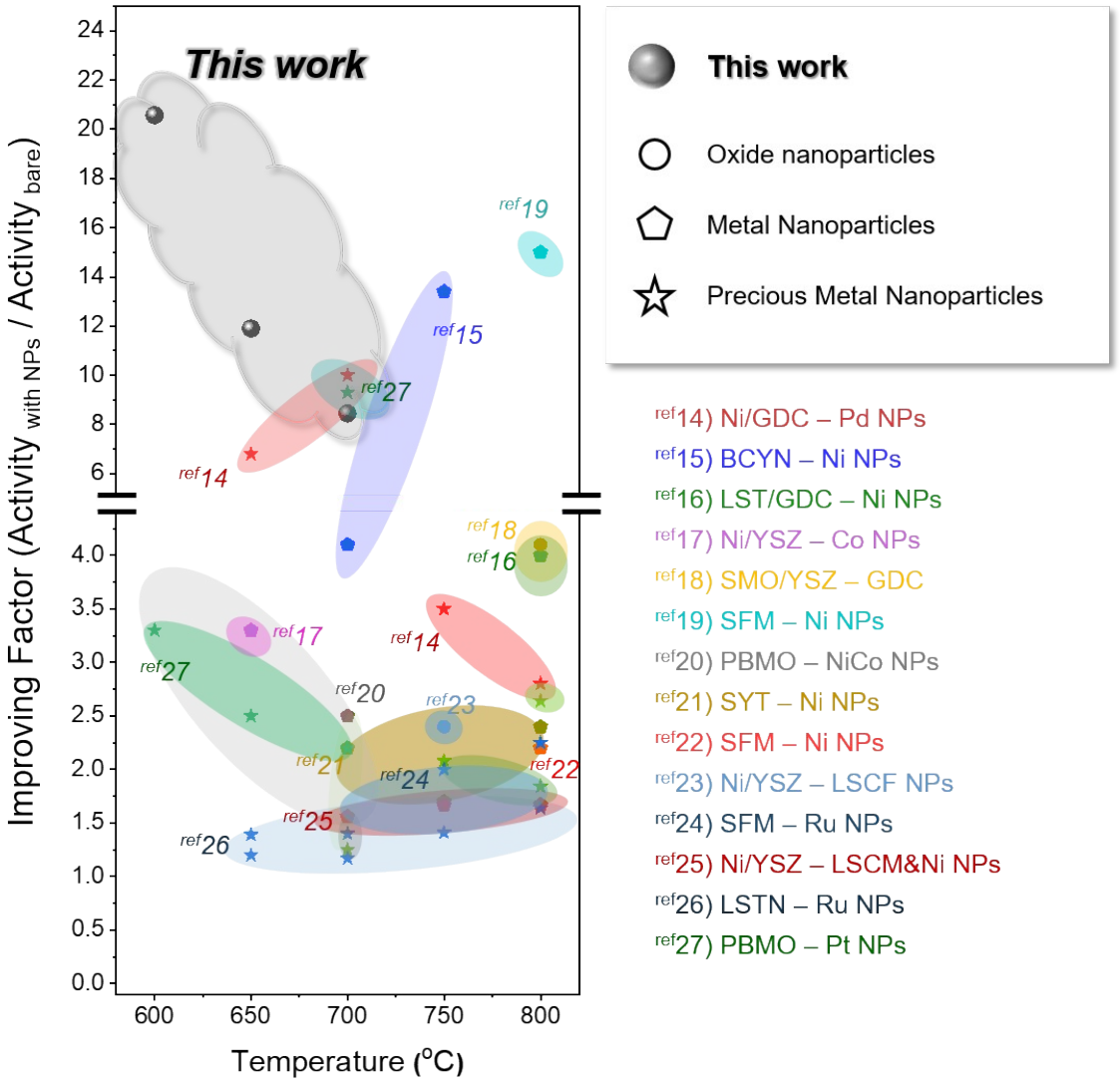

Figure S11. Comparison of improving factor (i.e., Activity$_{\text{, with NPs}}$ / Activity$_{\text{, bare anode}}$) with other literature applying nanoparticles to SOFC anode. [14–27]

References

[1] C. Wang, H. Daimon, T. Onodera, T. Koda, S. Sun, *Angewandte Chemie* **2008**, *120*, 3644.

[2] M. Zhao, Z. Chen, Z. Lyu, Z. D. Hood, M. Xie, M. Vara, M. Chi, Y. Xia, *J Am Chem Soc* **2019**, *141*, 7028.

[3] J. U. Bang, S. J. Lee, J. S. Jang, W. Choi, H. Song, *J Phys Chem Lett* **2012**, *3*, 3781.

[4] H. Winnischofer, T. C. R. Rocha, W. C. Nunes, L. M. Socolovsky, M. Knobel, D. Zanchet, *ACS Nano* **2008**, *2*, 1313.

[5] M. Saccoccio, T. H. Wan, C. Chen, F. Ciucci, *Electrochim Acta* **2014**, *147*, 470.

[6] H. W. Nesbitt, D. Banerjee, *American Mineralogist* **1998**, *83*, 305.

[7] D. Banerjee, H. W. Nesbitt, *Geochim Cosmochim Acta* **1999**, *63*, 3025.

[8] D. Banerjee, H. W. Nesbitt, *Geochim Cosmochim Acta* **1999**, *63*, 1671.

[9] D. Banerjee, H. W. Nesbitt, *Geochim Cosmochim Acta* **2001**, *65*, 1703.

[10] M. C. Biesinger, B. P. Payne, A. P. Grosvenor, L. W. M. Lau, A. R. Gerson, R. S. C. Smart, *Appl Surf Sci* **2011**, *257*, 2717.

[11] J. Seo, N. Tsvetkov, S. J. Jeong, Y. Yoo, S. Ji, J. H. Kim, J. K. Kang, W. C. Jung, *ACS Appl Mater Interfaces* **2020**, *12*, 4405.

[12] C. Macías-Sotelo, A. Cruz-López, S. I. Suárez-Vázquez, *Mater Chem Phys* **2019**, *228*, 194.

[13] S. Sengodan, S. Choi, A. Jun, T. H. Shin, Y. W. Ju, H. Y. Jeong, J. Shin, J. T. S. Irvine, G. Kim, *Nat Mater* **2015**, *14*, 205.

[14] A. Babaei, L. Zhang, E. Liu, S. P. Jiang, *Int J Hydrogen Energy* **2012**, *37*, 15301.

[15] Y. Liu, L. Jia, B. Chi, J. Pu, J. Li, *ACS Omega* **2019**, *4*, 21494.

[16] K. Bin Yoo, B. H. Park, G. M. Choi, *Solid State Ion* **2012**, *225*, 104.

[17] G. Yang, C. Su, W. Wang, R. Ran, M. O. Tadé, Z. Shao, *J Power Sources* **2014**, *264*, 220.

[18] P. Xiao, X. Ge, L. Zhang, J.-M. Lee, J.-Y. Wang, X. Wang, *Int J Hydrogen Energy* **2012**, *37*, 18349.

[19] G. Xiao, C. Jin, Q. Liu, A. Heyden, F. Chen, *J Power Sources* **2012**, *201*, 43.

[20] B. Hua, N. Yan, M. Li, Y.-F. Sun, Y.-Q. Zhang, J. Li, T. Etsell, P. Sarkar, J.-L. Luo, *Adv. Mater* **2016**, *28*, 8922.

[21] E. K. Park, S. Lee, J. W. Yun, *Appl Surf Sci* **2018**, *429*, 171.

[22] G. Xiao, F. Chen, *Electrochem commun* **2011**, *13*, 57.

[23] J. Mirzababaei, S. S. C. Chuang, *Catalysts* **2014**, *4*, 146.

[24] F. Hu, K. Chen, Y. Ling, Y. Huang, S. Zhao, S. Wang, L. Gui, B. He, L. Zhao, *Advanced Science* **2024**, *11*, 2306845.

[25] X. Zhu, Z. Lü, B. Wei, M. Liu, X. Huang, W. Su, *Electrochim Acta* **2010**, *55*, 3932.

[26] Y. Tang, H. Wang, R. Wang, Q. Liu, Z. Yan, L. Xu, X. Liu, *ACS Appl Mater Interfaces* **2022**, *14*, 44002.

[27] J. Seo, S. Jeon, S. Lee, D.-K. Lim, J. H. Kim, J. H. Kim, S. Ahn, W. Jung, *ACS Catal* **2022**, *12*, 8593.